Journal of Fluids and Structures 20 (2005) 659–672

JOURNAL OF
FLUIDS AND
STRUCTURES

www.elsevier.com/locate/jfs

Control of flow around a NACA 0012 airfoil with a micro-riblet film

S.-J. Lee*, Y.-G. Jang

Department of Mechanical Engineering, Pohang University of Science and Technology, Pohang 790-784, South Korea

Received 23 December 2003; accepted 4 March 2005
Available online 23 May 2005

Abstract

The flow structure of the wake behind a NACA 0012 airfoil covered with a V-shaped micro-riblet film (hereafter, MRF) has been investigated experimentally. The results were compared with the corresponding results from an identical airfoil covered with a smooth polydimethylsiloxane (PDMS) film of the same thickness. The drag force acting on each airfoil, as well as the spatial distributions of turbulence statistics in the near wake behind each airfoil, were measured for Reynolds numbers (calculated based on the chord length, $C = 75\,\text{mm}$) ranging from $\text{Re} = 1.03 \times 10^4$ to 5.14×10^4. At $\text{Re} = 1.54 \times 10^4$ ($U_0 = 3\,\text{m/s}$), the drag force on the MRF-covered airfoil was about 6.6% lower than that on the smooth airfoil. In contrast, at the higher Reynolds number of $\text{Re} = 4.62 \times 10^4$ ($U_0 = 9\,\text{m/s}$), application of the MRF increased the drag force by about 9.8%. To determine the spatial distributions of turbulence intensity, including the mean velocity, turbulence intensity and turbulent kinetic energy, 500 instantaneous velocity fields of the wake behind each airfoil were measured using a 2-frame PIV technique and ensemble averaged. For the case of drag reduction ($\text{Re} = 1.54 \times 10^4$), the near wake behind the MRF-covered airfoil had a shorter vortex formation region and higher vertical velocity component compared with that behind the smooth airfoil. At the downstream end of vortex formation region, the Reynolds shear stress and turbulent kinetic energy for the MRF-covered airfoil were similar or slightly larger than for the smooth airfoil. Smoke-wire flow visualization showed that the presence of the MRF on the airfoil surface caused the smoke filaments to become thinner and to be separated by a smaller lateral spacing, indicating suppression of spanwise movement. For the drag-increasing case ($\text{Re} = 4.62 \times 10^4$), the presence of MRF grooves on the airfoil seemed to increase the vertical velocity component and decrease the height of the large-scale streamwise vortices, which interacted actively. This active interaction increased the turbulent kinetic energy and Reynolds shear stress in the near-wake region, increasing the drag force acting on the airfoil.

Keywords: Flow control; Micro-riblet; Drag reduction; Cross-correlation PIV; NACA 0012 airfoil

---

1. Introduction

Drag reduction has attracted great interest in fluid mechanics research. Much of this interest has derived from the practical benefits of reducing drag; for example, reduction of the drag on transport vehicles leads directly to decreased fuel consumption and thus lowers operational costs. One flow control technique that has been shown to effectively

---

*Corresponding author. Tel.: +82 54 279 2169; fax: +82 54 279 3199.
E-mail address: sjlee@postech.ac.kr (S.-J. Lee).

0889-9746/$ - see front matter © 2005 Elsevier Ltd. All rights reserved.
doi:10.1016/j.jfluidstructs.2005.03.003

reduce drag on a body is texturing the surface of the body with longitudinal grooves (known as riblets) along the streamwise direction.

Several previous studies have shown that introduction of grooves onto a surface can reduce drag by changing the near-surface flow structure. In an investigation of several types of riblet surfaces, Walsh (1983) found that the drag was reduced under geometric conditions of $s^+ (= su_\tau/v) < 30$ and $h^+ (= hu_\tau/v) < 25$ (s^+ and h^+ defined in terms of wall units, s is the spacing of riblet grooves and h is the height of riblet tip) for V-shaped grooves. Bacher and Smith (1986) found that the streaks formed above a riblet-covered flat surface are wider than those above a flat plate, and that the flow within the riblet valleys is slow and quiescent. Bechert and Bartenwerfer (1989) simulated flow over various riblet configurations using the conformal mapping method and, based on the simulation results, hypothesized that the sharp ridges of riblets impede instantaneous cross-flow in the viscous sublayer and reduce the wall shear stress. Choi (1989) reported that the restriction of spanwise movement of longitudinal vortices contributes significantly to reduce the drag over riblet surfaces. Park and Wallace (1994) used a hot-wire probe to measure the streamwise velocity profiles over a surface with riblet grooves of $h^+ = 14$ and $s^+ = 28$. They found that, compared with flow over a smooth surface, the riblet surface exhibited 4% lower drag and the vertical flux of the streamwise momentum was reduced within the riblet valleys.

Choi et al. (1993) used direct numerical simulation (DNS) to simulate the flow structures over riblets in order to investigate the drag reduction mechanism. They found that when the riblet spacing s^+ is smaller than the size of the streamwise vortices, the drag is reduced due to the relatively small area affected by the down-wash motion of the streamwise vortices. Goldstein et al. (1995) attributed the drag reduction effect of riblets to the damping of cross-flow velocity fluctuations. Riblets spaced closely do not allow large streamwise vortices to settle inside the riblet valleys, whereas such vortices can reside in the valleys between widely spaced riblets.

Lee and Lee (2001) investigated the near-wall turbulent structure of flows over surfaces covered with riblets having semi-circular grooves for the drag-decreasing ($s^+ = 25.2$) and drag-increasing ($s^+ = 40.6$) cases. They measured 1000 consecutive instantaneous velocity fields over the riblet surface using a particle image velocimetry (PIV) velocity field measurement technique to obtain reliable turbulence intensity.

Suzuki and Kasagi (1994) investigated the flow structure over a V-shaped riblet surface using a 3-D particle tracking velocimetry (PTV) system. They reported that the drag reduction mechanism is closely related to the suppression of near-wall vortex generation and the damping of vortices. Djenidi and Antonia (1996) carried out LDA measurements of flow over a V-grooved riblet surface for the drag-decreasing ($s^+ = 25$) and drag-increasing ($s^+ = 75$) cases. They found that the near-wall secondary flow motions were much weaker in the drag-decreasing system compared to the drag-increasing system. Most previous studies on riblet surfaces have focused on the flow behavior over flat plates textured with macro-scale riblets. However, in practical applications such as vehicles moving at high speed, the riblet spacing s^+ should be reduced to the micro-scale and the riblet surface should be applied to curved bluff bodies such as airfoils. In the present study, a flexible micro-riblet film (referred to from this point onwards as MRF) was fabricated and applied to a symmetric NACA 0012 airfoil.

Caram and Ahmed (1991) found that application of micro-riblets of $s = 23$–$152\,\mu\text{m}$ to an airfoil reduced the drag by 2.7–13.3%. They used flexible MRF made of polyvinylidene fluoride that were fabricated by plastic rolling or casting processes. However, the surface condition of these riblet films was not so clean and the peaks were slightly blunt.

The main objectives of the present study were to investigate the flow characteristics of the near wake behind a NACA 0012 airfoil covered with MRF and to study the effect of using a MRF-covered surface on the drag. The usefulness of MRF attachment was assessed by analyzing the spatial distributions of the turbulence intensity of the wake behind the MRF-covered airfoil, which were measured using a high-resolution PIV system, and by comparing the results with the corresponding data for a smooth airfoil.

2. Experimental apparatus and method

2.1. Fabrication of the MRF

The MRF was fabricated according to the process described by Han et al. (2002). Briefly, the basic mold of a V-grooved micro-riblet was fabricated using an anisotropic etching technique. First, a silicon wafer was etched with TMAH as an anisotropic etchant, leading to the formation of V-grooves with a half-peak angle of 35.26° on the wafer surface. Two hundred V-grooves were formed on a wafer of dimensions 6 cm × 6 cm, as shown in Fig. 1. The height of each groove was 176.8 μm and the spacing between grooves was 300 μm. It is not easy to make uniform microstructure

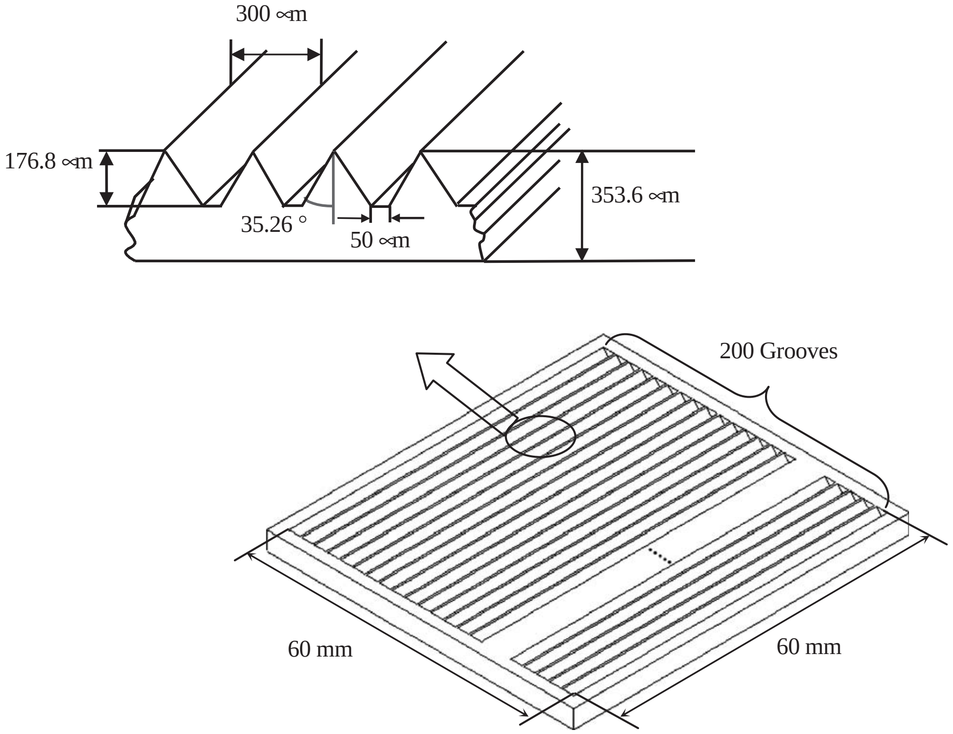

Fig. 1. Schematic diagram of a micro-riblet film (MRF).

arrays over a large area. For example, misalignment between the patterns on the ultra-violet (UV) mask and the crystal lines of the silicon wafer, or dislocations or impurities on the silicon wafer, can cause defects in the fabricated micro-grooves. To minimize such defects, we used a premium-grade silicon wafer and paid great attention to accurately aligning the UV mask and silicon wafer. The grooves on the silicon mold were replicated using a polydimethylsiloxane (PDMS) micro-molding technique to make several flexible MRFs. The resulting MRFs had sharp peaks and were flexible enough to attach onto any curved surface.

2.2. Experimental apparatus and method

The experiments were performed in a closed-type subsonic wind tunnel of test section 0.15 m (width) × 0.15 m (height) × 1.8 m (length). The turbulence intensity of the empty wind tunnel was less 0.1% at 7 m/s. The NACA 0012 airfoil model made of acryl has a chord length of $C = 75\,\mathrm{mm}$ and a thickness of 9 mm. The airfoil model was mounted in the middle height of the test section at zero angle of attack. During the experiments, the Reynolds number based on the airfoil chord length was varied in the range of $\mathrm{Re} = 1.03 \times 10^4$–$5.14 \times 10^4$.

Two airfoils of the same shape and size, but with different surface configurations, were tested in this study. One airfoil was covered with the MRF and the other was covered with a PDMS film of the same equivalent thickness. Since the MRF of about 300 μm in thickness is attached to the airfoil tightly, the original shape of the airfoil is nearly maintained. We paid a great deal of attention to aligning the riblet grooves along the free-stream direction.

The aerodynamic forces acting on the airfoil model were measured using a three-component load-cell (Nissho LMC-3502) with a nonlinearity of less than ±0.5% in the full range of $2\,\mathrm{kg_f}$. The load-cell having temperature sensitivity of 0.05%/°C was coupled with a DC strain amplifier (DSA-100). The precision error is less than 2%. The drag coefficient based on the effective frontal area (A) of the airfoil model was defined as follows:

$$C_D = \frac{\text{Drag}}{\frac{1}{2}\rho U_0^2 A}. \tag{1}$$

Instantaneous velocity fields of the wake behind the airfoil were measured using a high-resolution 2-frame PIV system consisting of an Nd:YAG laser, a 2 K × 2 K Kodak CCD camera and a delay generator, as shown in Fig. 2. The maximum pulse repetition rate of the laser was 15 Hz and its energy output was 125 mJ/pulse. Because the laser pulse had a short pulse width of about 7 ns, clear images of the turbulent eddy motions could be captured. A delay generator (BNC 555-2) was used to synchronize the Nd:YAG laser and CCD camera. The time interval Δt between consecutive laser pulses was also controlled using the delay generator. During the time interval Δt, particles move in and out of the laser light sheet. Therefore, it is necessary to adjust the thickness of the laser light sheet appropriately and to reduce the time interval as short as possible. However, the time interval Δt depends mainly on the maximum particle displacement in the interrogation window. In the present experiments, the laser light sheet was about 1 mm thick. For further details on the 2-frame PIV velocity field measurement system and its accuracy, we refer the reader to Lee (2001). Olive oil particles of approximately 1 μm in mean diameter were used as tracer particles. Because the blockage of the tunnel by the presence of airfoil model is about 6%, we did not correct the blockage effects on drag coefficient and flow speed.

PIV measurements were carried out on the NACA 0012 airfoil with and without MRF attached at two free-stream velocities, $U_0 = 3$ and 9 m/s. The corresponding Reynolds numbers, based on the airfoil chord length, are 1.54×10^4 and 4.62×10^4, respectively. These two free-stream velocities were chosen because they correspond to the conditions of maximum drag reduction and increase for the NACA 0012 airfoil, respectively. Instantaneous velocity fields inside two consecutive axial planes of the near wake were measured. Each field of view located in the middle plane of the test section was about $50 \times 50\,\text{mm}^2$ in physical dimension. The time interval Δt between consecutive pulses was set to 15–75 μs, depending on the flow condition.

A total of 500 instantaneous velocity fields were obtained for each experimental condition. This number of velocity fields was chosen based on preliminary tests. When 500 instantaneous velocity field data were averaged, the measurement error of streamwise mean velocity is less than 2%. The interrogation window size was 32 × 32 pixels, and

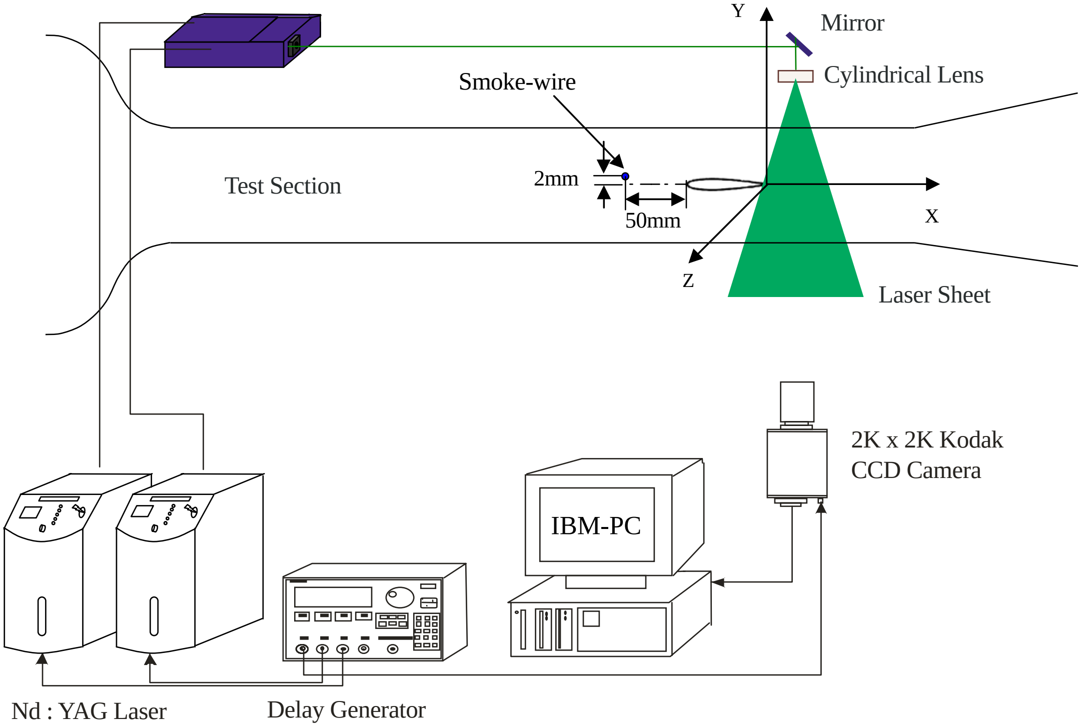

Fig. 2. Experimental set-up for PIV measurements and flow visualization with coordinate system.

the windows overlapped by 50%. By ensemble averaging the 500 instantaneous velocity vector fields, the spatial distributions of turbulence intensity were obtained.

The turbulent kinetic energy, k, was calculated using the following isotropic assumption,

$$\bar{w}^2 \approx \tfrac{1}{2}(\bar{u}^2 + \bar{v}^2),$$

$$k = \tfrac{1}{2}\rho(\bar{u}^2 + \bar{v}^2 + \bar{w}^2) \approx \tfrac{3}{4}\rho(\bar{u}^2 + \bar{v}^2). \tag{2}$$

Due to the assumption of an isotropic flow structure, the real turbulent kinetic energy may differ slightly from the present results in the regions in which the 3-D flow structure is anisotropic.

The flow structures around the airfoil model with and without MRF attached were visualized using a smoke-wire method. A fine nichrome wire (diameter 100 μm) was placed horizontally at a location about 50 mm ahead of the airfoil and 2 mm above the centerline, as shown in Fig. 2. Flow visualization experiments were carried out at four sections, specifically, one horizontal plane 1 mm above the airfoil and three vertical sagittal planes ($X = -15$, 2, and 15 mm). The field of view is smaller than that of PIV measurement to see the difference of flow structure in more detail.

When electric power was applied to the smoke-wire coated with SAFEX fog fluid, small droplets of SAFEX fluid evaporated to produce white smoke filaments. A thin laser light sheet produced by passing the pulsed laser through a cylindrical lens illuminated the smoke streaks, providing a qualitative picture of the instantaneous flow structure. Shortly before the laser firing, the shutter of the digital camera (Nikon D-100) was opened. To obtain clear flow images with good contrast, the pulsed Nd:YAG laser, digital camera and DC power supply were synchronized using a delay generator.

3. Results and discussion

3.1. *Drag force*

Fig. 3 shows the effect of attaching MRF onto the airfoil on the drag reduction rate with respect to the smooth airfoil as a function of Reynolds number. Here, C_{D_0} denotes the drag coefficient of the smooth airfoil. The drag coefficient (C_D) of the MRF-covered airfoil gradually decreases with increasing Reynolds number. The smooth airfoil shows a similar trend; however, its drag coefficient decreases at a greater rate than that of the MRF-covered airfoil. Therefore, the drag reduction achieved by MRF attachment is great at lower Reynolds numbers.

At Re = 1.54×10^4, the MRF-covered airfoil shows about 6.6% drag reduction, compared with the airfoil covered with smooth PDMS. In the range of Re = 2.57×10^4–3.08×10^4, the presence of the MRF induces no significant variation in the drag coefficient. At Re = 4.62×10^4, however, the attachment of MRF increases the drag coefficient by

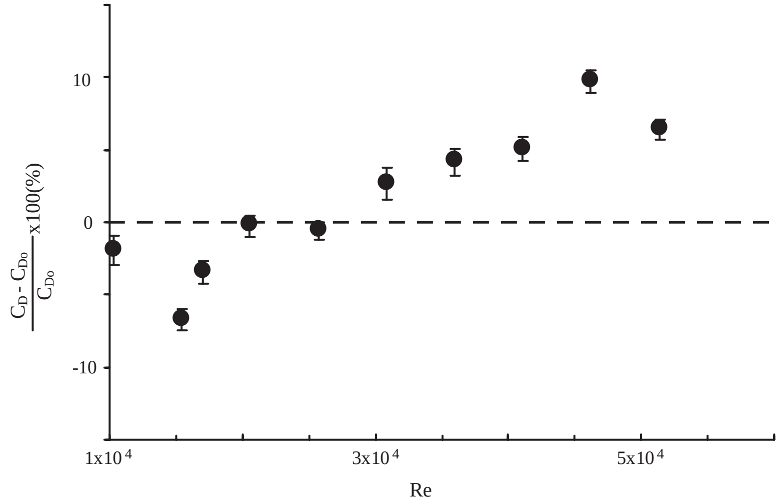

Fig. 3. Drag reduction with respect to smooth airfoil as a function of Reynolds number.

about 9.8%. For the case of riblets immersed in a flat plate boundary layer, drag reduction is mainly related with the size of the streamwise vortices. For the case of MRF-covered airfoil, however, in addition to the flow structure variation, the riblet grooves also modify the transition from laminar to turbulent flow. For a smooth NACA0012 airfoil, the critical Reynolds number for transition from laminar to turbulent flow has been known as $\mathrm{Re}_{\mathrm{cr}} = 10^5$–$10^6$. However, the presence of roughness over the airfoil surface makes the transition to occur at earlier Reynolds number (Dryden, 1953). Ladd et al. (1993) mentioned that the riblets promote and hasten transition relative to the flow over a smooth vinyl coated plate and affect the location of laminar-to-turbulent transition. The transition Reynolds number for the smooth flat plate was about 2.75×10^6 and those for the five tested riblets had lower values.

From simple comparison, the result of Suzuki and Kasagi (1994) for a flat plate, although the surface and flow conditions are different, can be used to estimate the riblet spacing s^+. The spacing s^+ is less than 15 at $U_0 = 3\,\mathrm{m/s}$ and larger than 30 at $U_0 = 9\,\mathrm{m/s}$. This indicates that the riblet grooves roughly satisfy the drag reduction condition of Walsh (1983). This indicates that in order to reduce drag effectively, the riblet geometry, especially the spacing between grooves, should be determined taking into consideration the flow speed. For a fixed flow speed, increasing the riblet spacing decreases the drag reduction effect of the riblet surface. To investigate the modification of the flow structure induced by attaching the MRF, the velocity fields of the near wake behind the airfoil with and without MRF were measured by 2-frame PIV.

3.2. *Mean velocity fields*

The velocity fields of the wake behind the MRF-covered airfoil were measured at the freestream velocities of $U_0 = 3$ and $9\,\mathrm{m/s}$, which correspond to maximum drag reduction ($\mathrm{Re} = 1.54 \times 10^4$) and maximum drag increase ($\mathrm{Re} = 4.62 \times 10^4$). Experiments under the same conditions were carried out using an identical airfoil covered with a smooth PDMS surface. The spatial distributions of the turbulence intensity of the wake were obtained by ensemble averaging 500 instantaneous velocity fields.

Fig. 4 shows the mean streamwise velocity distribution in the longitudinal vertical plane for the MRF- and PDMS-covered airfoils subjected to flow velocities of $\mathrm{Re} = 1.54 \times 10^4$ and $\mathrm{Re} = 4.62 \times 10^4$. In all systems, the contours are nearly symmetric with respect to the wake centerline ($y = 0$). For the case of $\mathrm{Re} = 1.54 \times 10^4$, at which the drag reduction induced by MRF attachment is maximum, the length of the vortex formation region behind the MRF-covered airfoil is shorter and the wake width is slightly longer, compared with the flow around the smooth airfoil. The end of the vortex formation region is usually determined as the point that has the maximum amount of streamwise velocity fluctuation along the wake centerline. These observations indicate that the riblet grooves trip the laminar flow and recover the velocity deficit more quickly with enhanced entrainment of inviscid flow into the wake region.

At $\mathrm{Re} = 4.62 \times 10^4$, however, the size of the velocity deficit region just behind the MRF-covered airfoil is larger than that behind the smooth airfoil. In addition, the width of the entire wake is larger than that of the smooth airfoil. The deficit of the streamwise mean velocity in the wake center is larger in the downstream of the vortex formation region.

Fig. 5 depicts the streamwise mean velocity profiles extracted from the ensemble-averaged mean velocity field at the downstream locations of $X/C = 0.3$ and 1.0. At $\mathrm{Re} = 1.54 \times 10^4$, the maximum velocity deficit of the smooth airfoil at $X/C = 0.3$ is about 17% larger than that of the MRF-covered airfoil. We estimated the profile drag from the wake velocity profile using the momentum theorem to compare with the total drag measured directly. The two drag results are in a good agreement. This indicates that a reduction of the velocity deficit in the near wake mainly causes a decrease in the drag coefficient. At the further downstream location of $X/C = 1.0$, the difference between the streamwise mean velocity profiles for the two surface types is much less, with the wake width of the MRF-covered airfoil being only slightly larger than that of the smooth airfoil. For the Reynolds number giving maximum drag increase ($\mathrm{Re} = 4.62 \times 10^4$), on the other hand, the MRF-covered airfoil has a larger velocity deficit than the smooth airfoil at both $X/C = 0.3$ and 1.0. At $X/C = 0.3$, the centerline streamwise velocity is about 9% smaller for the MRF-covered airfoil compared to the smooth airfoil.

Fig. 6 shows the spatial distributions of the vertical mean velocity component for the MRF- and PDMS-covered airfoils at $\mathrm{Re} = 1.54 \times 10^4$ and 4.62×10^4. Similar to the streamwise velocity field data (Fig. 4), the spatial distributions of the vertical mean velocity component are almost symmetric with respect to the wake centerline ($y = 0$). The vertical velocity component has small values inside the vortex formation region, irrespective of the Reynolds number. At $\mathrm{Re} = 4.62 \times 10^4$, the vertical velocity component in the shear layer around the vortex formation region is larger for the riblet-covered airfoil than for the smooth airfoil. Strong vertical transport of momentum into the wake region causes active turbulent mixing and increase turbulent kinetic energy, increasing drag force acting on the airfoil.

The vertical velocity component in the near wake region at $\mathrm{Re} = 1.54 \times 10^4$ is slightly larger for the MRF-covered airfoil than for the smooth airfoil. It indicates that the riblet grooves enhance the entrainment of inviscid flow into the

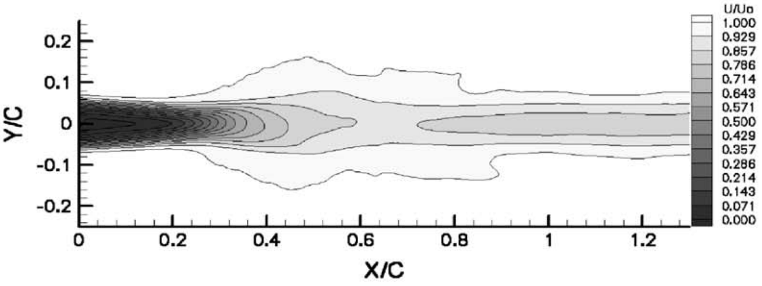

(a) MRF airfoil Re=1.54×10^4

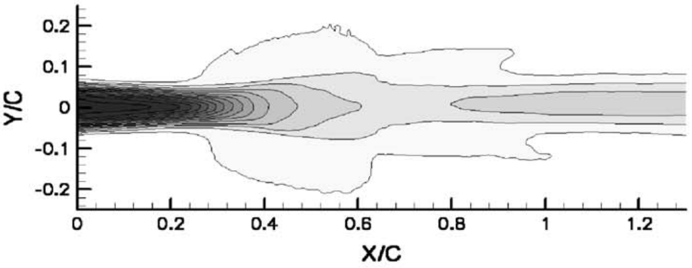

(b) smooth airfoil Re=1.54×10^4

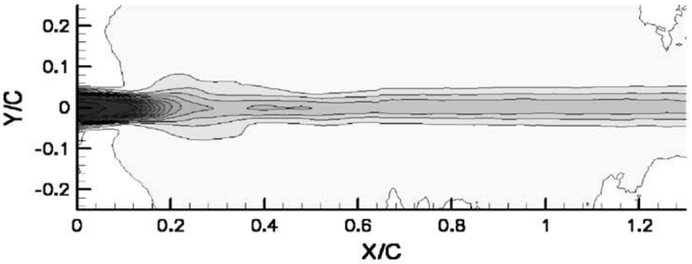

(c) MRF airfoil Re=4.62×10^4

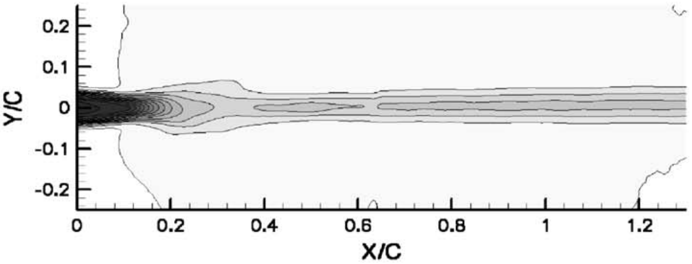

(d) smooth airfoil Re=4.62×10^4

Fig. 4. Mean streamwise velocity distributions in the longitudinal plane.

wake region just behind the airfoil, expanding the wake width and decreasing the velocity deficit, and ultimately result in reduction of the drag force. Comparison of the vertical velocity distributions in the $\mathrm{Re} = 1.54 \times 10^4$ flows around the MRF-covered and smooth airfoils (Figs. 6(a) and (b), respectively) discloses that the vortex formation region behind the MRF-covered airfoil is shorter and wider than that behind the smooth airfoil. At the higher Reynolds number of $\mathrm{Re} = 4.62 \times 10^4$, the streamwise vortices seem to actively interact with the grooves of the MRF surface (Fig. 6(c)), increasing the magnitudes of the vertical velocity component and drag coefficient. From the $\mathrm{Re} = 1.54 \times 10^4$ data in Figs. 4 and 6, we find that the flow around the MRF-covered airfoil is characterized by a smaller velocity deficit and

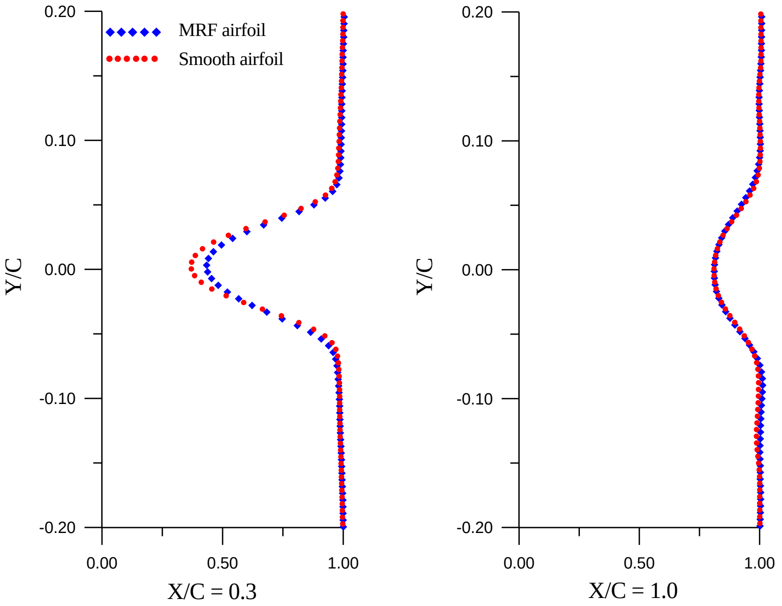

(a) Re =1.54 x10^4 (U$_0$ = 3m/s)

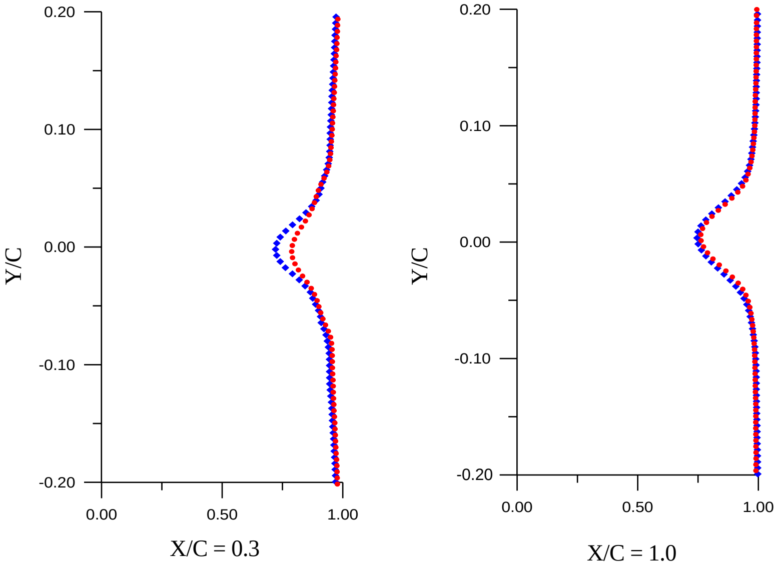

(b) Re = 4.62 x10^4 (U$_0$ = 9m/s)

Fig. 5. Comparison of mean streamwise velocity profiles at downstream locations.

larger vertical entraining velocity in the near wake region, compared with the smooth airfoil flow. These differences may be attributed to the suppression of the spanwise movement of streamwise vortices by the riblet grooves.

Fig. 7 shows the spatial distributions of turbulent kinetic energy for the MRF- and PDMS-covered airfoils at Re = 4.62 × 10^4 and 1.54 × 10^4. For the drag reduction case (Re = 1.54 × 10^4), the turbulent kinetic energy in the flow around the MRF-covered airfoil is predominantly similar to that for the smooth airfoil, except for slightly larger values at the end of the vortex formation region. For the drag-increasing case (Re = 4.62 × 10^4), however, the turbulent kinetic energy in the wake center region just behind the vortex formation region is of much greater magnitude for the

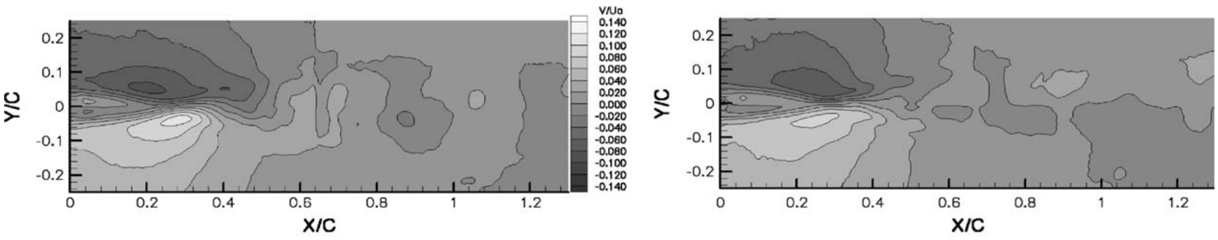

(a) MRF airfoil Re=1.54×10^4 (b) smooth airfoil Re=1.54×10^4

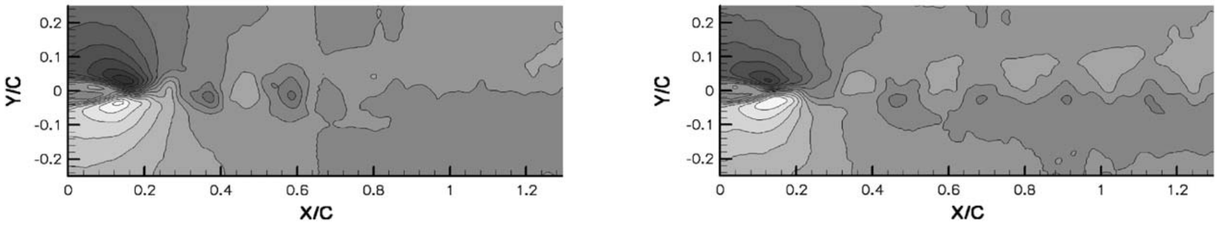

(c) MRF airfoil Re=4.62×10^4 (d) smooth airfoil Re=4.62×10^4

Fig. 6. Contour plots of vertical mean velocity in the longitudinal plane.

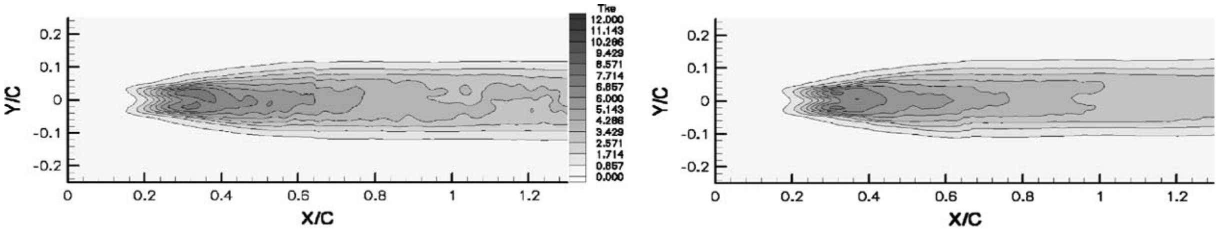

(a) MRF airfoil Re=1.54×10^4 (b) smooth airfoil Re=1.54×10^4

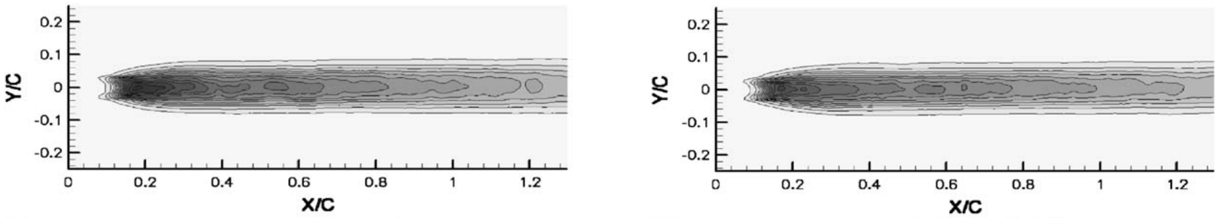

(c) MRF airfoil Re=4.62×10^4 (d) smooth airfoil Re=4.62×10^4

Fig. 7. Variation of turbulent kinetic energy distribution.

MRF-covered airfoil than for the smooth airfoil. The greater degree of turbulent fluctuations in the flow around the MRF-covered airfoil seems to be closely related to the strong vertical flow motion induced by the presence of the V-shaped micro-riblet grooves. The riblet grooves seemed to act as surface roughness at higher Reynolds number.

The variation of the Reynolds stress distribution is shown in Fig. 8. The Reynolds stress distribution of flows around the two types of airfoil show similar global structure. At $\mathrm{Re} = 1.54 \times 10^4$, however, if we check it carefully, the Reynolds stress has slightly larger values in the region behind the vortex formation region of the MRF-covered airfoil compared to the corresponding region behind the smooth airfoil. On going to the higher Reynolds number of $\mathrm{Re} = 4.62 \times 10^4$, the MRF airfoil has higher Reynolds shear stress in the smaller area behind the airfoil, compared to the smooth airfoil. It is interesting to note that the peak values in the turbulent kinetic energy and Reynolds shear stress distributions appear at almost the same location. The Reynolds shear stress is large only in the region behind the vortex formation region, and thereafter it decreases rapidly. In contrast, the turbulent kinetic energy decreases slowly due to slow dissipation of the flow.

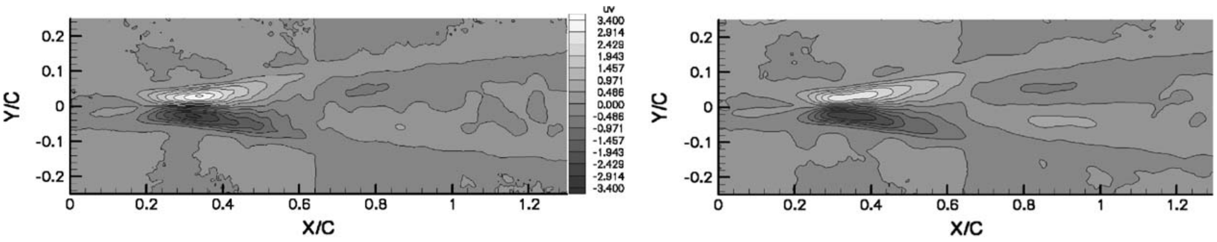

(a) MRF airfoil Re=1.54×10^4

(b) smooth airfoil Re=1.54×10^4

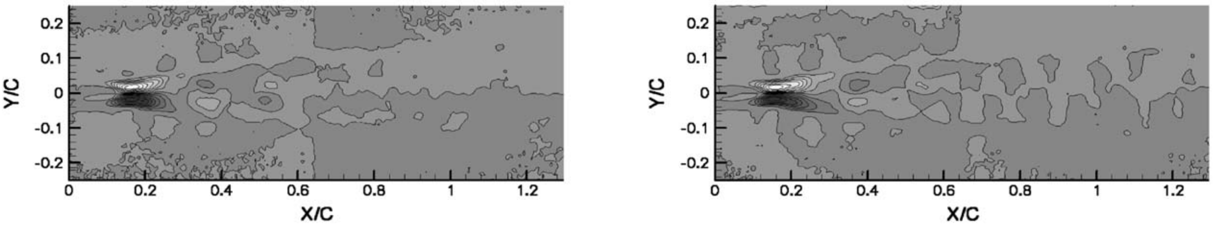

(c) MRF airfoil Re=4.62×10^4

(d) smooth airfoil Re=4.62×10^4

Fig. 8. Variation of Reynolds shear stress distribution.

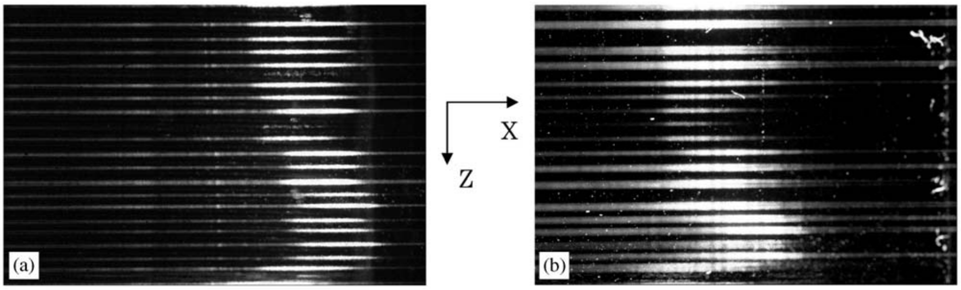

MRF airfoil (Re=1.54×10^4)

smooth airfoil (Re=1.54×10^4)

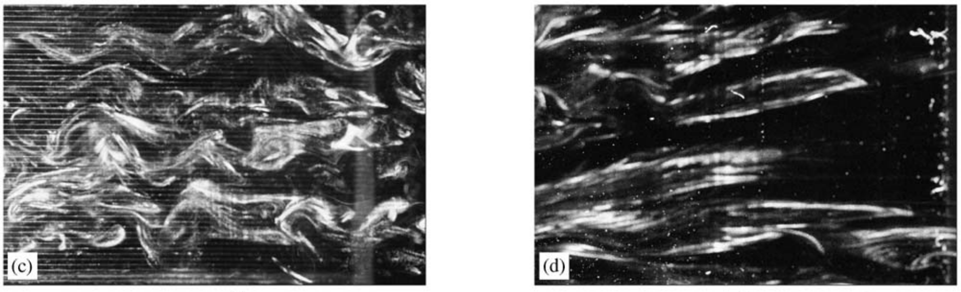

MRF airfoil (Re=4.62×10^4)

smooth airfoil (Re=4.62×10^4)

Fig. 9. Flow images visualized in a horizontal plane above the airfoil.

Further study is needed to investigate in detail the way in which the micro-scale flow structure just above a surface is modified by the presence of micro-riblets.

3.3. Flow visualization

Fig. 9 shows visualizations of the flow in a horizontal plane about 1 mm above the airfoil model. At Re $= 1.54 \times 10^4$, the flows around the two types of airfoil both show a straightforward streak pattern. However, the smoke filaments are

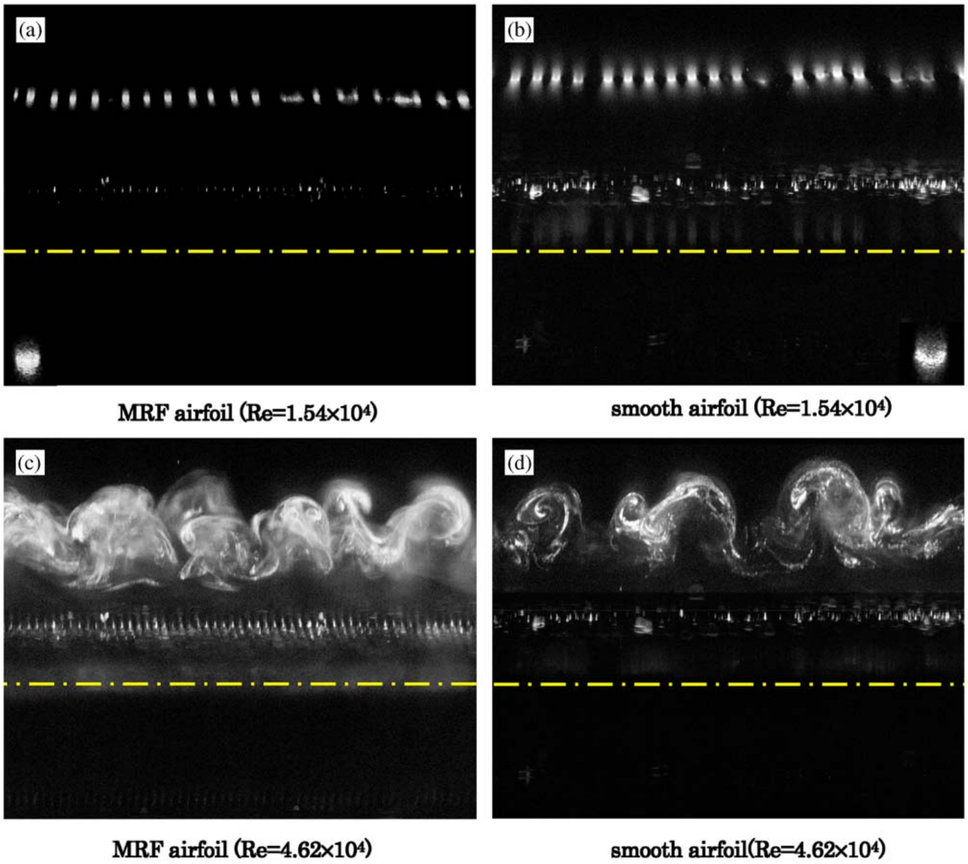

Fig. 10. Visualized flow in the spanwise vertical cross-section at $X = -15$ mm.

thicker and the streak spacing is wider in the flow above the smooth airfoil compared to that above the MRF-covered airfoil. The wider streak spacing indicates some degree of active spanwise momentum transport above the smooth airfoil. At $\mathrm{Re} = 4.62 \times 10^4$, the visualized flow above the MRF airfoil shows a complicated streak structure entangled with streamwise vortices.

Sagittal flow images visualized in the vertical cross-section above the airfoil at $X = -15$ mm are shown in Fig. 10. At $\mathrm{Re} = 1.54 \times 10^4$, the streak spacing is smaller in the flow above the MRF airfoil than in that above the smooth airfoil. The streak spacing seems to be influenced mainly by the riblet grooves, especially the riblet tips. The shorter streak spacing indicates suppression of spanwise momentum transport and stabilization of low-speed streak due to the presence of riblet grooves. On the other hand, the smoke filaments formed above the smooth airfoil have a half-loop shape due to active spanwise momentum transport. Another notable characteristic of these flow images is that, although the smoke-wire was positioned at the same location when recording the images, the streak height for the MRF airfoil is about 7 mm, lower than the height (8 mm) for the smooth airfoil. This indicates that the MRF grooves change the transition from laminar to turbulent flow and enhance the entrainment of inviscid ambient fluid into the wake center. The increased vertical velocity component seems to be caused by the increase of flow speed along the riblet valley. This phenomenon, which is supported by the data in Fig. 6, enhances vertical momentum transport, thereby reducing the vortex formation region and the drag force acting on the MRF airfoil compared with the smooth airfoil.

At $\mathrm{Re} = 4.62 \times 10^4$, the flow above the MRF airfoil contains smaller streamwise vortices, densely distributed along the spanwise direction, compared to the flow above the smooth airfoil, which contains large, sparsely distributed vortices. In addition, similar to the behavior at $\mathrm{Re} = 1.54 \times 10^4$, the vertical distance to the streamwise vortices from the airfoil is smaller for the MRF airfoil than for the smooth airfoil.

Fig. 11 shows smoke filaments visualized in the vertical cross-section just behind the airfoil at $X = 2$ mm. These visualized flow patterns are similar to those recorded at $X = -15$ mm, even though they are separated from the airfoil. For the case of drag reduction ($\mathrm{Re} = 1.54 \times 10^4$), the MRF airfoil does not give rise to large-scale vortices and the

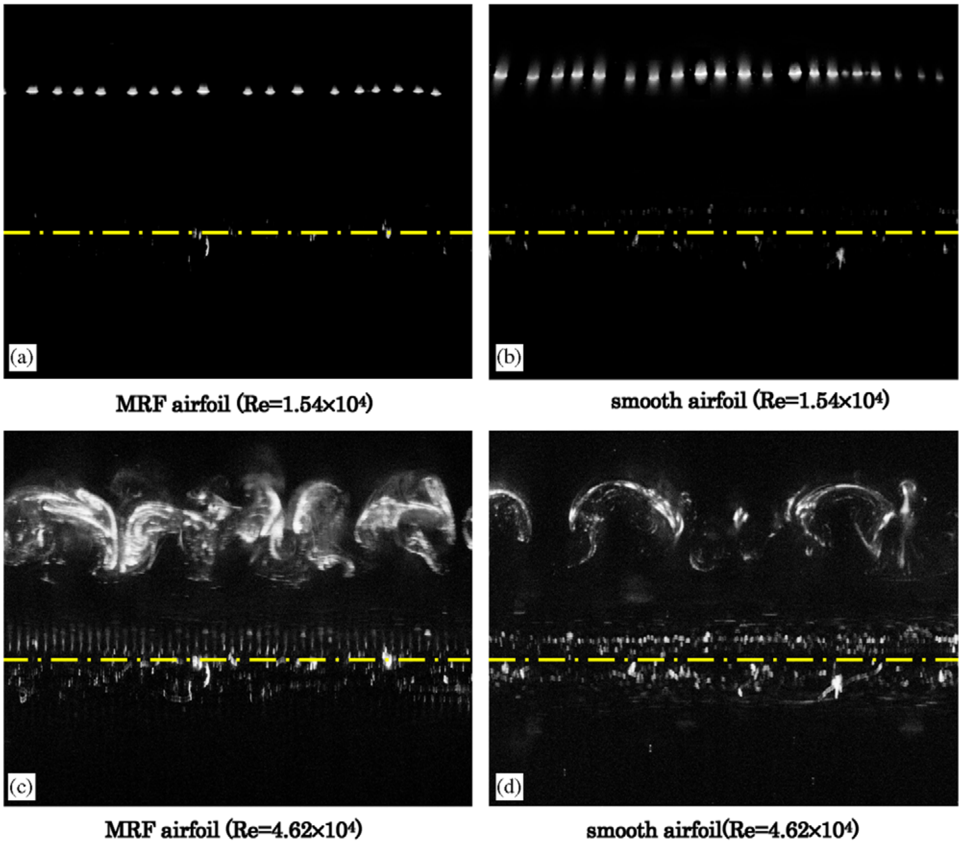

Fig. 11. Visualized flow in the spanwise vertical cross-section at $X = 2\,\text{mm}$.

smoke filaments are densely distributed due to the suppression of spanwise momentum transport. At $\text{Re} = 4.62 \times 10^4$, the flow above the MRF airfoil contains large-scale streamwise vortices that are densely packed and interact actively. This results from the fact that riblet grooves act as surface roughness at this higher Reynolds number. The active interaction may enhance the turbulent kinetic energy, increasing the Reynolds shear stress and eventually increasing the drag force. In contrast, the flow around the smooth airfoil at $\text{Re} = 4.62 \times 10^4$ is comprised of large-scale, sparsely distributed streamwise vortices.

Fig. 12 shows sagittal flow images in the vertical plane at $X = 15\,\text{mm}$. At $\text{Re} = 1.54 \times 10^4$, the height of smoke streak is largely reduced than the smooth airfoil, indicating that the MRF airfoil causes vertical flow motion. At $\text{Re} = 4.62 \times 10^4$, vortices formed behind the MRF airfoil interact actively; these vortices are located at the wake center due to active vertical momentum transport. In contrast, the vortices that form behind the smooth airfoil are larger in size, do not show active interaction, and are located away from the wake center, even at $X = 15\,\text{mm}$.

The above results indicate that the introduction of MRF grooves onto a smooth airfoil surface causes strong vertical movement toward the wake centerline and reduces the size of the vortex formation region. However, when the MRF-covered airfoil is subjected to higher flow speeds, the riblet grooves act as surface roughness and streamwise vortices are actively interacted, enhancing the turbulent kinetic energy and Reynolds shear stress, and increasing the drag force. In contrast, the smooth airfoil displayed a relatively simple vortex structure in the near wake under high flow speeds.

4. Conclusions

A flexible MRF fabricated by a MEMS technique was applied to the surface of a NACA 0012 airfoil to investigate the effect of micro-riblets on drag. Measurements of the drag force using a three-component load-cell showed that the MRF grooves reduced the drag coefficient by about 6.6% at $U_0 = 3\,\text{m/s}$ ($\text{Re} = 1.54 \times 10^4$), compared with the smooth

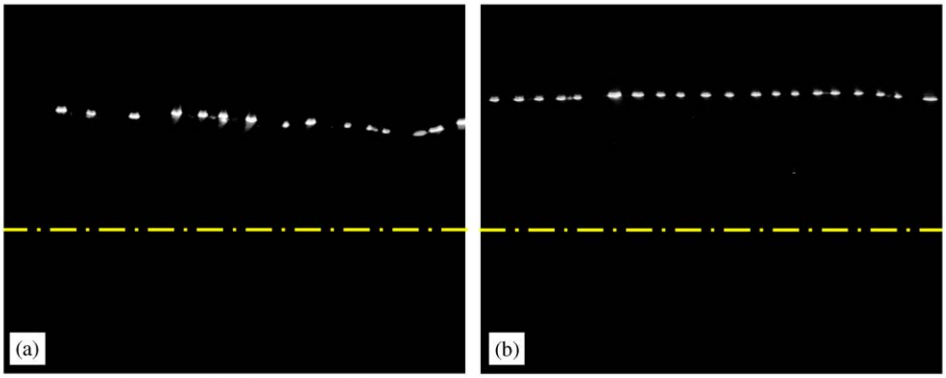

MRF airfoil (Re=1.54×10⁴) smooth airfoil (Re=1.54×10⁴)

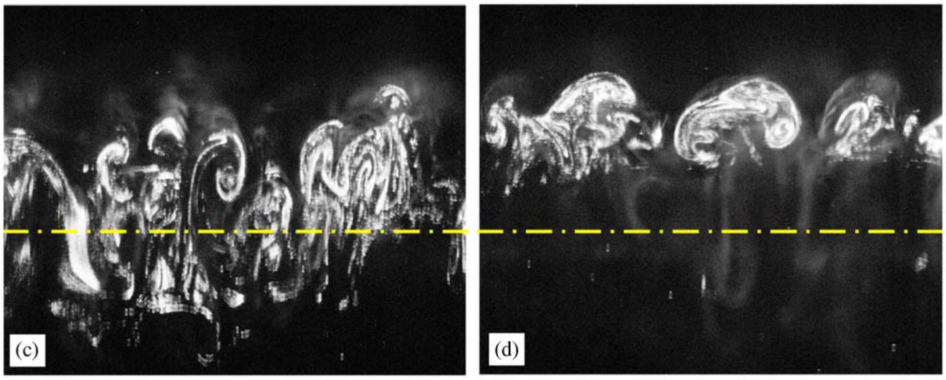

MRF airfoil (Re=4.62×10⁴) smooth airfoil (Re=4.62×10⁴)

Fig. 12. Visualized flow in the spanwise vertical cross-section at $X = 15\,\text{mm}$.

airfoil. At $U_0 = 9\,\text{m/s}$ ($\text{Re} = 4.62 \times 10^4$), however, application of MRF to the airfoil increased the drag coefficient by about 9.8%.

The mean velocity fields of the near wake behind the smooth and MRF-covered airfoils were measured at freestream velocities of 3 and 9 m/s using a PIV velocity field measurement technique. Compared with the smooth airfoil, the MRF-covered airfoil had a larger vertical velocity component in the near-wake region ($X/L < 0.2$), which enhanced the entrainment of ambient fluid into the wake. At the higher Reynolds number ($\text{Re} = 4.62 \times 10^4$), the riblet grooves acting as surface roughness interacted actively with the streamwise vortices, leading to an increase in the sizes of the vortex formation region, the velocity deficit region, and the wake width. At the lower Reynolds number ($\text{Re} = 1.54 \times 10^4$), the riblet grooves seemed to trip the laminar flow and recover the velocity deficit more quickly than the smooth airfoil. The vortex formation length was reduced by introducing micro-riblets onto the smooth airfoil surface.

Smoke-wire flow visualization revealed that the MRF grooves suppress spanwise momentum transport and enhance the vertical velocity component. At $\text{Re} = 1.54 \times 10^4$, the streak filaments become thinner and move towards the wake center due to enhancement of the vertical velocity by the micro-riblets. For the drag increasing case ($\text{Re} = 4.62 \times 10^4$), the MRF grooves attached to the airfoil worked as surface roughness and led to a more complicated vortex structure in which smaller-scale streamwise vortices were densely distributed and interacted actively. This active interaction of vortices caused a substantial increase in the turbulent kinetic energy, leading to a higher drag force on the airfoil.

Acknowledgement

This research was supported by National Research Laboratory (NRL) program of Ministry of Science and Technology (MOST), Korea.

References

Bacher, E.V., Smith, C.R., 1986. Turbulent boundary layer modification by surface riblets. American Institute of Aeronautics and Astronautics Journal 24, 1382–1385.

Bechert, D.W., Bartenwerfer, M., 1989. The viscous flow on surfaces with longitudinal ribs. Journal of Fluid Mechanics 206, 105–129.

Caram, J.M., Ahmed, A., 1991. Effect of riblets on turbulence in the wake of an airfoil. American Institute of Aeronautics and Astronautics Journal 29, 1769–1770.

Choi, H.C., Moin, P., Kim, J., 1993. Direct Numerical Simulation of turbulent flow over riblets. Journal of Fluid Mechanics 255, 503–539.

Choi, K.S., 1989. Near-wall structure of a turbulent boundary layer with riblets. Journal of Fluid Mechanics 208, 417–458.

Djenidi, L., Antonia, R.A., 1996. Laser Doppler anemometer measurements of turbulent boundary layer over a riblet surface. American Institute of Aeronautics and Astronautics Journal 34, 1007–1012.

Dryden, H.L., 1953. Review of published data on the effect of roughness on transition from laminar to turbulent flow. Journal of the Aeronautical Sciences 20, 477–482.

Goldstein, D., Handler, R., Sirovich, L., 1995. Direct Numerical Simulation of turbulent flow over a modeled riblet covered surface. Journal of Fluid Mechanics 302, 333–376.

Han, M.H., Huh, J.G., Lee, S.S., Lee, S.J., 2002. Micro-riblet film for drag reduction. Proceedings of the Pacific Rim Workshop on Transducers & Micro/Nano Technologies, Xiamen, China, July 22–24, pp. 47–50.

Ladd, D.M., Rohr, J.J., Reidy, L.W., Hendricks, E.W., 1993. The effect of riblets on laminar to turbulent transition. Experiments in Fluids 14, 1–9.

Lee, S.J., 2001. PIV/PTV Velocity field measurement technique—theory and practice. PIV'2001 Lecture Note, POSTECH.

Lee, S.J., Lee, S.H., 2001. Flow field analysis of a turbulent boundary layer over a riblet surface. Experiments in Fluids 30, 53–166.

Park, S.R., Wallace, J.M., 1994. Flow alteration and drag reduction by riblets in a turbulent boundary layer. American Institute of Aeronautics and Astronautics Journal 32, 31–38.

Suzuki, Y., Kasagi, N., 1994. Turbulent drag reduction mechanism above a riblet surface. American Institute of Aeronautics and Astronautics Journal 32, 1781–1790.

Walsh, M.J., 1983. Riblets as a viscous drag reduction technique. American Institute of Aeronautics and Astronautics Journal 21, 485–486.